nature communications

Article

https://doi.org/10.1038/s41467-025-68195-1

Filament assembly induced by the recognition of target DNA activates the prokaryotic Argonaute SPARDA system

Received: 20 July 2025

Accepted: 19 December 2025

Published online: 06 January 2026

Check for updates

Wanyue Zhang[1,4], Yuchen Jiang[2,3,4], Yu Li[2,3,4], Xiangkai Zhen[1,4], Shuying Xu[1], Ning-shao Xia[2,3], Shaowei Li[2,3] ✉, Xurong Wang[1] ✉, Qingbing Zheng[2] ✉ & Songying Ouyang[1] ✉

The short prokaryotic Argonaute (pAgo) proteins, in conjunction with their associated effector molecules, constitute a defence mechanism in prokaryotes that protects against phage infections. The SPARDA is characterized by its collateral nuclease activity, which, upon activation through target DNA recognition, non-specifically cleaves a wide range of nucleic acid substrates. Nevertheless, the structural underpinnings of its collateral activity have remained elusive. In this study, we investigate the *Nba*SPARDA system from *Novosphingopyxis baekryungensis* and reveal that RNA-guided DNA recognition triggers the assembly of a higher-order filamentous structure. This filamentation is essential for the tetramerization of the DREN nuclease domain, which in turn facilitates the accumulation and cleavage of substrate nucleic acids. Through the determination of the gRNA-bound and RNA-DNA duplex-bound cryo-EM structures, we delineate a sequential monomer-dimer-monomer-filament transition during SPARDA activation. These insights collectively elucidate a filament-dependent activation mechanism underpinning the short pAgo-mediated immune response, which is crucial for antiviral defence.

Argonaute (Ago) proteins are a conserved family that is widely distributed across all domains of life. Eukaryotic Ago (eAgo) combines with 22-nt guide RNA (gRNA) to form the essential component of the RNA-induced silencing complex (RISC) in the RNA interference (RNAi) pathway, which silences the target RNA that is paired to the gRNA[1,2]. Extensive structural studies on Ago have demonstrated that canonical eAgo is composed of four structural domains (N, PAZ, MID, and PIWI), which are connected by two linkers (L1 and L2)[3,4]. The MID and PAZ domains are responsible for the binding of the 5′ and 3′ ends of gRNA and target DNA (tDNA), respectively[5]. The RNase H fold of PIWI possesses a DEDX catalytic triad to cleave the target. The architecture of eAgo displays a bilobed conformation in which the N and PAZ domains form one lobe, whereas the MID and PIWI domains form the other lobe[6,7]. The guide–target heteroduplex is bound in the central channel formed by the N-PAZ and MID-PIWI lobes[8].

Unlike eAgo, the roles of their homologues in prokaryotes (pAgo) are not fully understood, despite pAgo being widely found in prokaryotes and archaea[9,10]. Compared with eAgo, pAgo is more diverse in

[1]Key Laboratory of Microbial Pathogenesis and Interventions of Fujian Province University Provincial University, the Key Laboratory of Innate Immune Biology of Fujian Province, Biomedical Research Center of South China, College of Life Sciences, Fujian Normal University, Fuzhou 350117, China. [2]State Key laboratory of vaccines for infectious diseases, Xiang An Biomedicine laboratory, School of life Sciences, School of Public health, Xiamen University, Xiamen, China. [3]National institute of diagnostics and vaccine development in infectious diseases, collaborative innovation center of Biologic Products, national innovation Platform for industry-education integration in vaccine Research, Xiamen University, Xiamen, China. [4]These authors contributed equally: Wanyue Zhang, Yuchen Jiang, Yu Li, Xiangkai Zhen. ✉e-mail: shaowei@xmu.edu.cn; William_wong@fjnu.edu.cn; qbzheng@xmu.edu.cn; ouyangsy@fjnu.edu.cn

terms of its domain composition and role in target cleavage[5,10]. Moreover, short pAgo is the largest group of pAgo, accounting for more than 60%[10]. However, short pAgo has only the MID domain and a catalytically inactive PIWI domain, which has led to the loss of its ability to cleave target nucleic acids[10]. Interestingly, recent studies revealed that short pAgo and neighbouring genes that encode fusion versions of proteins with a C-terminal APAZ (Analogue of PAZ) domain and diverse N-terminal effectors, including TIR, Sir2, and DUF3457, function together as antiviral systems in response to phage infection[10,11]. Furthermore, pAgo-related systems can be classified into four categories, in which the mechanisms used to defend against phage infection are distinct[11–13]. To date, the mechanisms underlying the majority of short pAgo-mediated antiphage have been elusive. Among the short pAgo systems, cellular NAD^+ was rapidly depleted in the SPARTA[14–18] and SPARSA[19–22] systems because of the recognition of the tDNA of the gRNA in the positively charged channel formed by the APAZ and the pAgo. In the three-component pAgo of *Sulfolobus islandicus* (SiAgo), the activation of the associated transmembrane Aga2 effector can result in membrane depolarization and cell death[23].

The SPARDA (Short Prokaryotic Argonaute and DNAse/RNase-Endonuclease) antiviral system is a newly identified antiphage system in which APAZ is fused with a nuclease domain [24,25]. Unlike eAgo proteins, in which the PIWI nuclease domain specifically cleaves paired targets[6], SPARDA of *Novosphingopyxis baekryungensis* (*Nba*SPARDA) and *Thermocrispum municipal* (*Tm*uSPARDA) unexpectedly exhibited collateral nuclease activity against various nucleic acid substrates dependent on the DREN nuclease domain upon target recognition[24,25]. However, the detailed mechanism of the assembly mechanism and the activation of the collateral indiscriminate nuclease activity of the DREN remains to be investigated. In this study, we demonstrate that fully paired tDNA can induce SPARDA filament formation; furthermore, we employ cryogenic electron microscopy (cryo-EM) to elucidate the tDNA-induced filament assembly of *Nba*SPARDA. A comparison of assembled and unassembled SPARDA structures reveals that filament assembly stabilizes the nuclease effector DREN and creates a binding channel for the substrate. Interestingly, the heteroduplex formed by gRNA and its complementary tDNA is located within the DREN domain, demonstrating the essential role of filament formation in activating SPARDA's collateral nuclease activity.

Results

Overall structure of the gRNA-bound SPARDA

SPARDA comprises a short pAgo and the cognate DREN–APAZ (Fig. 1A), which can assemble into a heterodimer[24]. To investigate the SPARDA assembly mechanism, we first attempted to determine its apo structure using cryo-EM. Size-exclusion chromatography (SEC) and SDS-PAGE analyses confirmed the stable heterodimer formation between pAgo and its cognate DREN–APAZ (Supplementary Fig. 1A, B). Analytical ultracentrifugation (AUC) of the sample yielded a molecular weight of 114 kDa (Supplementary Fig. 1C), consistent with the SEC findings and indicative of a 1:1 stoichiometric complex similar to those of other pAgo homologues[17–19,21,26]. Unfortunately, preferential orientation during cryo-EM visualization hindered the structural resolution of SPARDA (Supplementary Fig. 2).

Based on an earlier study in which gRNA and complementary tDNA can induce the collateral nuclease activity of SPARDA[24], we incubated a precise 20-nt gRNA with purified SPARDA to form the gRNA–SPARDA complex. Consistent with prior findings, the introduction of paired tDNA enabled the processing of a wide spectrum of substrates, including ssDNA, dsDNA and RNA (Fig. 1B). Cryo-EM analysis of the gRNA–SPARDA complex revealed a significant improvement in sample homogeneity with the addition of gRNA. Surprisingly, 2D classification indicated that gRNA-bound SPARDA adopted a dimeric conformation, distinct from the monomeric state of apo SPARDA (Supplementary Fig. 3). SEC analysis confirmed the formation of the gRNA–SPARDA complex (Supplementary Fig. 4A). Accordingly, the AUC results of gRNA–SPARDA yielded a calculated molecular weight of approximately 200 kDa (Supplementary Fig. 4B), which also reconfirmed that gRNA induces dimerization of SPARDA.

Finally, we resolved the cryo-EM structure of the gRNA–SPARDA complex at 2.77 Å resolution (Fig. 1C, D). The final map revealed that the N-terminal DREN nuclease domain was not visible, likely because of high flexibility, whereas only the first six nucleotides of the seed region of the gRNA could be traced (Fig. 1D), possibly because the remainder is solvent exposed, akin to the homologues in Ago proteins[14,19]. The structure contains two pAgo subunits and two copies of the cognate DREN–APAZ (Fig. 1D).

Like conventional Ago family homologues, each pAgo subunit adopts a canonical architecture, comprising an N-terminal MID domain (residues 1–250) and a C-terminal PIWI domain (residues 251–485). Although the DREN domain was not visible, the C-terminal APAZ domain (residues 161–442) presents a classical mixed α/β fold that resembles those in other short pAgo homologues[7]. The APAZ domain is positioned to the PIWI domain, forming a characteristic heterodimer with a buried interface of approximately 1,200 $Å^2$. Overall, the APAZ–pAgo heterodimer has an architecture similar to that of previous pAgo-related systems, generating a positively charged cavity to accumulate nucleic acids (Supplementary Fig. 5). Structural analysis revealed that the β1-strand, along with the C-terminal β12 and β11 strands protruding from the APAZ domain, forms a hand-like fold to lock the PIWI domain of pAgo (Fig. 1E). Hydrogen-bonding contacts were identified such that H410 from the last β-sheet of APAZ forms hydrogen bonds with T5 located in the nearby β-sheet of the MID domain. Residues L165 and N167 from the β1-β2 loop of APAZ establish hydrogen bonds with L376 and R374 located in the surrounding loop of the PIWI domain. In addition, R326 of the β11-sheet of APAZ forms a hydrogen bond with T372 in the PIWI domain (Fig. 1E). Complementary hydrophobic packing further reinforces the interface.

Like typical Ago family proteins, the gRNA is bound within the MID domain of both pAgo–APAZ heterodimers. In addition, Mg^{2+} was coordinated between the 5′-phosphate of the gRNA and the phosphate group of the third nucleotide (adenine) (Fig. 1F), providing a structural basis for the previously observed inability of SPARDA to cleave substrates in the absence of Mg^{2+}[24]. The 5′-phosphate group is further recognized by the side chains of R183 and K240 in the MID domain (Fig. 1G), which is consistent with the conserved arginine–lysine motif in typical Ago proteins[5,7]. The first adenine of the gRNA is inserted into a hydrophobic pocket formed by aromatic amino acids W159, W201 and F182 in the MID domain and establishes a hydrogen bond with the side chain of N181 (Fig. 1G). The second nucleotide, U2, forms hydrogen bonds with the side chains of Q224 and N232, whereas A3 interacts with Q224. Notably, the 2′-OH groups of U2, A3, and C4 form hydrogen bonds with multiple residues in the MID domain (Fig. 1G), potentially explaining the preference of SPARDA for RNA over ssDNA as a guide[24].

Structural basis for the dimerization assembly of SPARDA induced by gRNA

The addition of gRNA promoted the dimerization of the SPARDA heterodimer. We subsequently performed structural analysis on the interfaces between the individual SPARDA heterodimers. Cryo-EM structure analysis revealed that gRNA binding repositions the two APAZ domains in a head-to-tail orientation (Fig. 2A), facilitating the formation of hydrogen bonds. In the APAZ interfaces, Q353 forms a hydrogen bond with the side chain of R260, and F354 packs against F202 to form π–π stacking interactions. Identical interactions occur at the symmetrical interface of the opposing APAZ domain (Fig. 2B). Similarly, the two pAgo subunits adopt a head-to-tail orientation mediated primarily by their PIWI domains. In particular, three loops protruding from the β-sheet core of each PIWI domain drive

https://doi.org/10.1038/s41467-025-68195-1

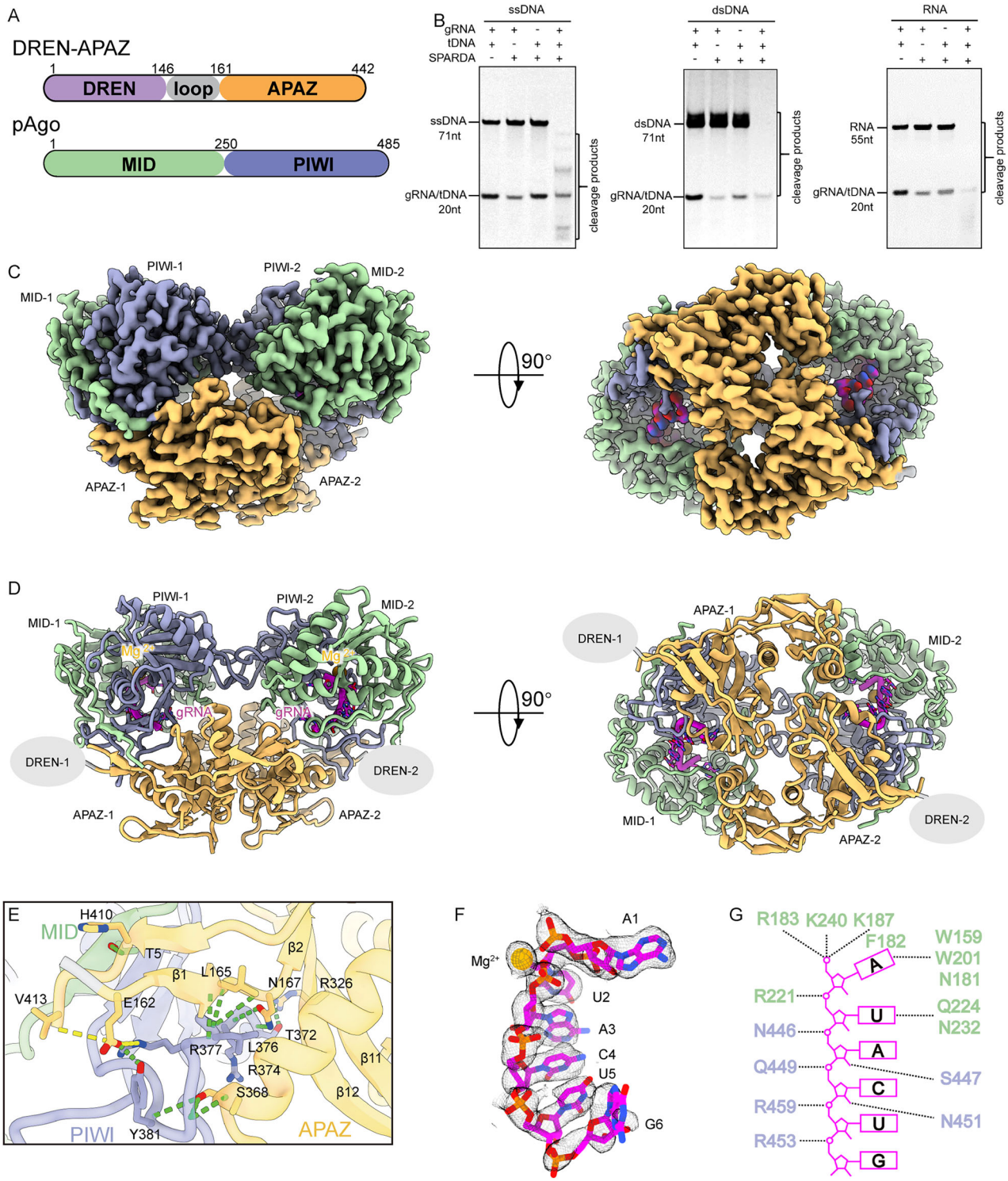

Fig. 1 | Cryo-EM structure of gRNA-bound SPARDA. A Domain organization of short pAgo and the DREN–APAZ of *Nba*SPARDA with residue numbers indicated below. **B** The purified SPARDA can cleave substrates of ssDNA (left), dsDNA (middle) and RNA (right) in the presence of gRNA and tDNA. Representative gels from three independent experiments, which produced similar results, are shown. **C** Cryo-EM reconstruction of the gRNA-bound SPARDA with individual domains is coloured in (**A**), and the gRNA is coloured in magenta. **D** Overall structures of the gRNA-bound SPARDA with each subunit are coloured individually; the N-terminal DREN is missing because of its flexibility. **E** Interactions between APAZ and pAgo. **F** The density of gRNA; Mg^{2+} is shown as a sphere. **G** Recognition mode of the gRNA and the MID domain of pAgo.

dimerization. Loop1 (residues 166–181), Loop2 (residues 265–275) and Loop3 (residues 293–338) facilitate these interactions. Specifically, R301 in Loop1 of pAgo1 forms hydrogen bonds with the side chains of E170 and T168 and the main chain of G176 in Loop3 of pAgo2. Additionally, T298 and A296 in Loop1 of pAgo1 establish hydrogen bonds with Q272 and Q273 in Loop2 of pAgo2, with similar interactions observed between the Loop1 of pAgo2 and the Loop2 and Loop3 in pAgo1 (Fig. 2C).

To investigate the role of gRNA-induced dimerization in regulating the collateral nuclease activity of SPARDA, we performed

https://doi.org/10.1038/s41467-025-68195-1

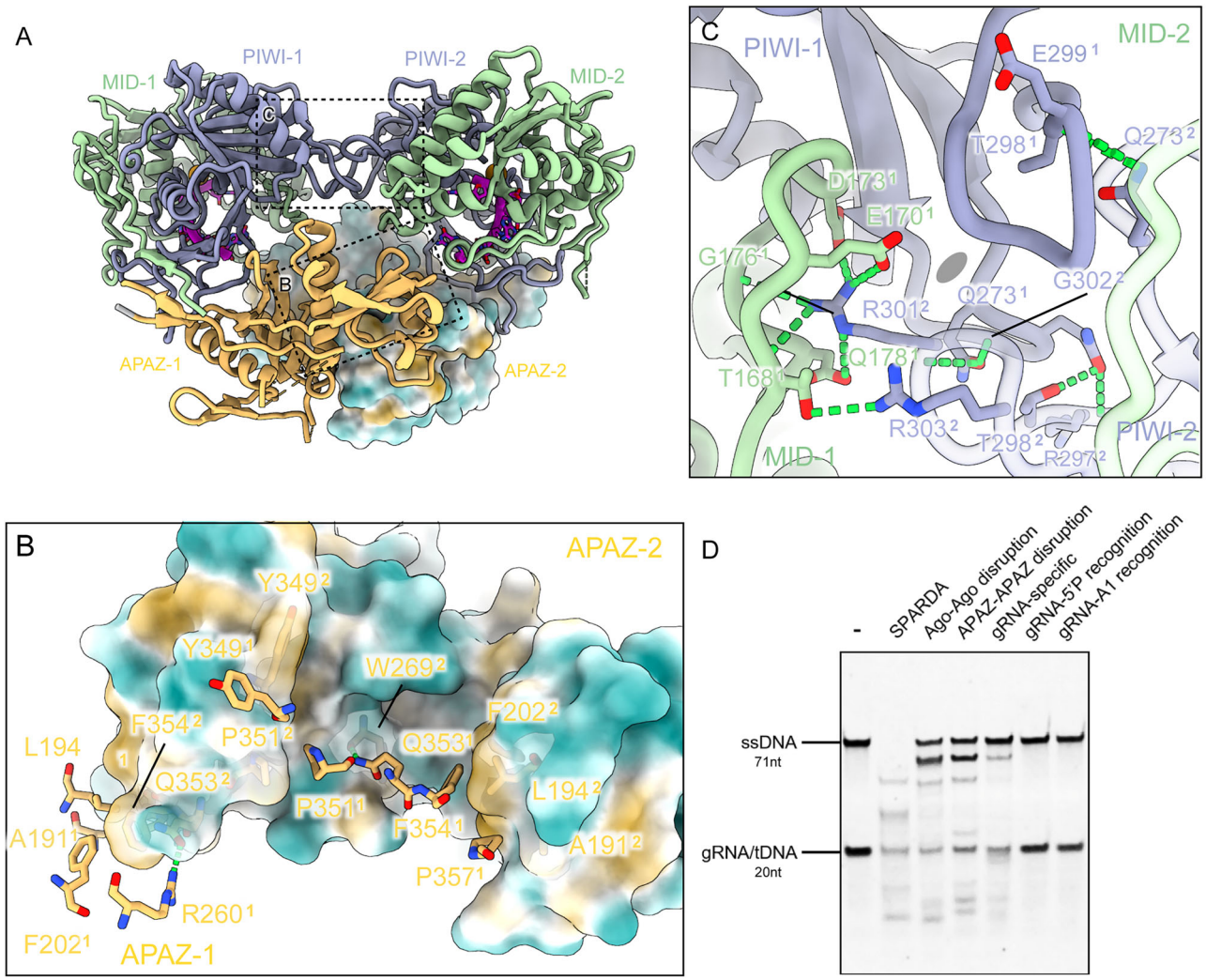

Fig. 2 | Structural basis for the dimerization of SPARDA induced by gRNA. **A** Overall structure of the gRNA-bound SPARDA complex. **B** APAZ–APAZ interfaces within the gRNA-bound dimeric SPARDA; the residues involved in the hydrogen bond and the hydrophobic interactions are shown as sticks and surfaces. **C** PIWI–PIWI interfaces within the gRNA-bound dimeric SPARDA; the residues involved in the interactions are shown as sticks. Hydrogen bonds are indicated by green lines. **D** Collateral activity of *Nba*SPARDA and the mutants with ssDNA. The gel image is representative of three independent experiments with similar results.

site-directed mutagenesis targeting key amino acids in SPARDA. Substitution of R183A/K187A/K240A, which are involved in the recognition of the 5′-phosphate group within the MID domain, significantly impaired SPARDA's nuclease activity. Similarly, mutations in gRNA-binding sites critical for A1 recognition (F182A/N181A/W159A/W201A) or 2′-OH contacts (S447A/N451A) abolish the nuclease activity of SPARDA (Fig. 2D). To assess whether gRNA-triggered dimerization is necessary for SPARDA nuclease activity, we simultaneously mutated the residues involved in the APAZ–APAZ interfaces and those at the interface between pAgo–pAgo subunits. Nuclease activity assays demonstrated that simultaneous mutation of these critical residues nearly abolished the ability of SPARDA to cleave nucleic acid substrates (Fig. 2D). Collectively, these findings indicate that gRNA-induced dimerization is essential for SPARDA activation.

tDNA recognition induces the formation of SPARDA filaments

To further elucidate the mechanism of DREN activation upon tDNA recognition of the gRNA, we initially incubated purified SPARDA with gRNA and complementary tDNA. However, no density for the gRNA–tDNA duplex was observed in the final map. We inferred that the gRNA–tDNA heteroduplex failed to be loaded in the SPARDA. Thus, we implemented an annealing step by heating the gRNA and tDNA to 95 °C for 2 minutes and then slowly cooling it to room temperature. The annealed gRNA–tDNA duplex was added to SPARDA at a ratio of 1:2 and subjected to cryo-EM. Unexpectedly, 2D classification (Supplementary Fig. 6) revealed that the micrographs exhibited regular helical filaments in all views, indicating that tDNA triggered the formation of a filamentous architecture in SPARDA (Fig. 3A). Analysis by size SEC and AUC demonstrated that gRNA–tDNA–SPARDA forms a supramolecular complex with a molecular mass of ~3.28 MDa (Supplementary Fig. 7A, B). Accordingly, in vitro nuclease activity assays established that collateral cleavage activity is exclusively observed in the high-molecular-weight fraction corresponding to the filamentous form (Supplementary Fig. 7C). In vivo BiFC assays further showed that SPARDA assembles into filamentous structures upon exogenous plasmid challenge (Supplementary Fig. 8). Collectively, these results suggested that tDNA recognition of the gRNA induces filament formation in SPARDA.

To better understand the link between SPARDA filamentation and collateral nuclease activity, we determined the structure of the complex of SPARDA bound to the gRNA and tDNA duplex through cryo-EM at 2.64 Å. The structure revealed that the activated SPARDA complex

https://doi.org/10.1038/s41467-025-68195-1

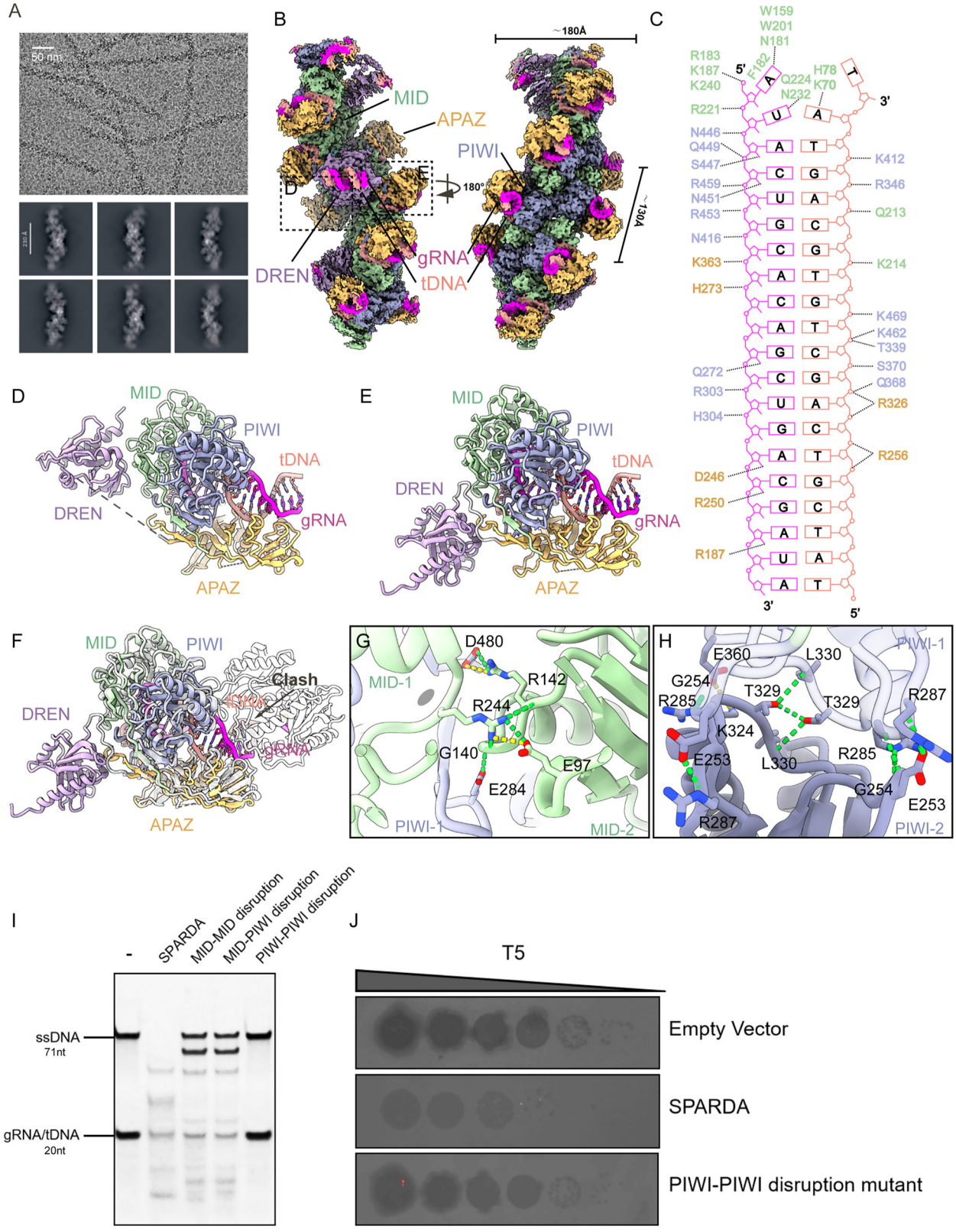

assembles into a regular helical filament with a helicase rise of approximately 130 Å and a diameter of approximately 180 Å (Fig. 3B). Each repeating unit of the SPARDA filament comprises four pAgo and four associated APAZ-DREN proteins. The four pAgo molecules are arranged as the backbone of the filament, whereas the cognate APAZ domains are pointed to the periphery of the filament (Fig. 3B). Notably, the N-terminal DREN domains, previously unresolved in inactive SPARDA, were unambiguously modelled within the SPARDA filament, where they were held together to further assemble into a tetrameric configuration (Fig. 3B). As observed in other Ago family proteins[8,17,19], tDNA and gRNA are bound within a specific nucleic acid-binding lobe formed by pAgo and the APAZ domain.

In the gRNA–tDNA-bound filamentous SPARDA complex, the 20-nt gRNA and its complementary tDNA could be traced (Fig. 3B, C).

Fig. 3 | Structural basis for the filament formation of SPARDA by tDNA. (**A**) Representative micrograph (top) and two-dimensional classes (bottom) of gRNA–tDNA-bound SPARDA; scale bar, 50 nm. Representative images of one from three independent experiments with similar results. **B** The helical filament of gRNA–tDNA-bound SPARDA, the central MID and PIWI of pAgo and the peripheral DREN–APAZ are indicated; the gRNA and tDNA are coloured in magenta and light coral. **C** Diagram of the *Nba*SPARDA and nucleic acid interactions (indicated with dashed lines). **D**, **E** The two different states of DREN with respect to the pAgo–APAZ; the dashed line represents the missing linker connecting the two domains. **F** Overlaid structures of DREN–APAZ and the pAgo heterodimer SPARDA in the complex of gRNA–tDNA and the gRNA-bound SPARDA dimer; the clash between the gRNA–tDNA heteroduplex and the MID domain of SAPRDA is indicated. **G** MID–PIWI and MID–MID interfaces within the SPARDA filament; the residues that participate in interactions are shown as sticks. Hydrogen bonds and salt bridges are indicated by green and orange dashed lines, respectively. **H** The PIWI–PIWI interfaces within the SPARDA filament; the residues that participate in hydrogen bond formation are shown as sticks. **I** Collateral activity of *Nba*SPARDA and the mutants with ssDNA. The gel image is representative of three independent experiments with similar results. **J** Bacterial growth assay showing the effects of wild-type *Nba*SPARDA and the mutants against infections by T5 phage.

Consistent with the recognition mode in the canonical Ago protein, the gRNA forms near-complete Watson–Crick base pairing with the tDNA, except for the first two 5′-terminal nucleotides. The 5′ phosphate of gRNA inserts into a binding pocket within the MID domain, while the remaining nucleotides extend into solvent-exposed regions, accounting for the lack of discernible density beyond this region. Overall, the recognition pattern between gRNA and tDNA is similar to that of other Ago family proteins in which the 5′ end of gRNA binds within the nucleic acid binding pocket of the MID domain, while other nucleotides are solvent exposed. The 3′ terminus of tDNA is anchored between the MID of pAgo and the APAZ domain, whereas its 5′ end extends towards the solvent-facing direction of the APAZ domain. The recognition of gRNA depends on base-specific recognition, which primarily relies on the 5′-terminal nucleotides of gRNA and the residues located in the MID domain of pAgo, and the nonspecific backbone contacts between the phosphate groups of the gRNA/tDNA backbones and the resides across the nucleic acid binding tunnel (Fig. 3C).

Structural basis for the formation of SPARDA filaments

In the SPARDA filament, pAgo serves as the backbone, with the basic structural unit comprising four pAgo molecules. Two central pAgo molecules are oriented towards each other through their MID domains (Fig. 3B). However, the DREN–APAZ subunits exhibit two distinct states: an extended state and a compact state. In the extended conformation, the DREN and APAZ domains are separated by a distance of approximately 20 Å, resulting in no density for the connecting linker (Fig. 3D). Conversely, in the compact state, the linker folds back towards the DREN domain, enabling clear observation of its density (Fig. 3E). Superimposition of the dimeric SPARDA and the compact-state pAgo–DREN–APAZ of the SPARDA filament revealed obvious steric hindrance between the guide-target heteroduplex and the other pAgo molecule in the dimeric SPARDA complex (Fig. 3F), suggesting that the dimeric of gRNA-bound SPARDA transformed into a monomer, which then formed a filament during the propagation of guide-target duplex. In comparison with the pAgo in the gRNA-bound dimeric SPARDA and the core dimeric pAgo in the filamentous SPARDA reveals a substantial structural rearrangement. Superimposition of one pAgo molecule in the dimeric SPARDA and that within the SPARDA filament, it could be observed a rotation of approximately 90 degrees in the other molecule. In the gRNA-bound dimeric SPARDA complex, dimer formation is primarily mediated by interactions between the PIWI domains of adjacent pAgo molecules. In contrast, within the activated SPARDA filament, the dimer interface is largely reconfigured and stabilized predominantly by interactions between the MID domains of adjacent molecules, as well as through amino acid contacts formed between the PIWI domain of one subunit and the MID domain of its neighbouring subunit.

Despite the overall structural similarity of pAgo and DREN–APAZ in the gRNA-bound SPARDA and the SPARDA filament, subtle local differences were observed, primarily in regions responsible for nucleic acid binding in pAgo and the C-terminal portion in DREN–APAZ. In particular, the region comprising residues 160–178 in pAgo, which was invisible in the gRNA-bound SPARDA, was stabilized by the binding of tDNA (Supplementary Fig. 9A). In addition, the loop containing residues 269–302, which is crucial for nucleic acid recognition, undergoes significant reorientation (Supplementary Fig. 9A). In filamentous SPARDA, this loop was extended outwards in active SPARDA, which ultimately formed the PIWI–PIWI interface that is essential for filamentation. Local conformational changes were also observed in the region responsible for gRNA 3′-end binding of APAZ, enabling coordination with the extended tDNA strand during filament formation (Fig. 3F).

At the MID–MID interface, R244 forms hydrogen bonds with the backbone of G140 and the side chains of R142 and E97 (Fig. 3G). The central pAgo molecule interacts with adjacent Ago molecules through the MID and the PIWI domains (Fig. 3G). The PIWI domain of pAgo engages with the MID domain of neighbouring pAgo, while the MID domain connects to the PIWI domain of another Ago. At the PIWI–MID interface, G140 and R142 form hydrogen bonds with E284 and D480 (Fig. 3G). In the PIWI–PIWI interaction interface, K324 participates in a charged interaction with E360, R287 forms another charged interaction with E253, and R285 establishes a hydrogen bond with G254; additionally, T329 and L330 form hydrogen bonds between the symmetric residues (Fig. 3H).

To investigate the functional significance of these interfaces, we introduced alanine substitutions at key residues within the MID–MID (E97A/G140A/R142A/R244 A) and MID–PIWI (G140A/R142A/E284A/D480A) interfaces and evaluated the impact of these mutations on SPARDA using in vitro collateral cleavage assays. The results indicated that individual mutations had negligible effects, whereas simultaneously mutating key residues in both the MID–MID and MID–PIWI interfaces impaired SPARDA's nuclease activity (Fig. 3I). Given that pAgo forms the backbone of the SPARDA filament, the conformational changes in the 269–302 region are likely to be critical for SPARDA filament assembly formation. Therefore, we introduced mutations into amino acids mediating PIWI–PIWI interactions within this region. Individual mutations did not markedly affect SPARDA function; however, simultaneous mutation of R285, R287, and K324 disrupted substrate cleavage and abolished the system's ability to confer resistance against bacteriophage infection (Fig. 3I, J). Collectively, these results demonstrate that tDNA-induced SPARDA filament formation occurs in the active form, which is essential for its collateral nuclease activity.

Mechanism of the activation of the DERN nuclease effector

The DREN domain (residues 1–145) is connected to the C-terminal APAZ domain by a flexible loop (146–166). In contrast, in the activated SPARDA filament assembly, the DREN domain can be modelled. The DREN domain is composed of seven β-strands surrounded by three α-helices. In each repeating unit of SPARDA, four DREN protomers assemble into a tetramer with D2 symmetry (Fig. 4A, B). However, the nuclease catalytic sites (E16, D41, Q60, and K62) of the two extended DREN-2 and 3 protomers (displayed as translucent surfaces) are positioned to the pocket formed by the tetramer; in contrast, the catalytic sites of the other DREN-1 and 4 (displayed as cartoons) are buried and

https://doi.org/10.1038/s41467-025-68195-1

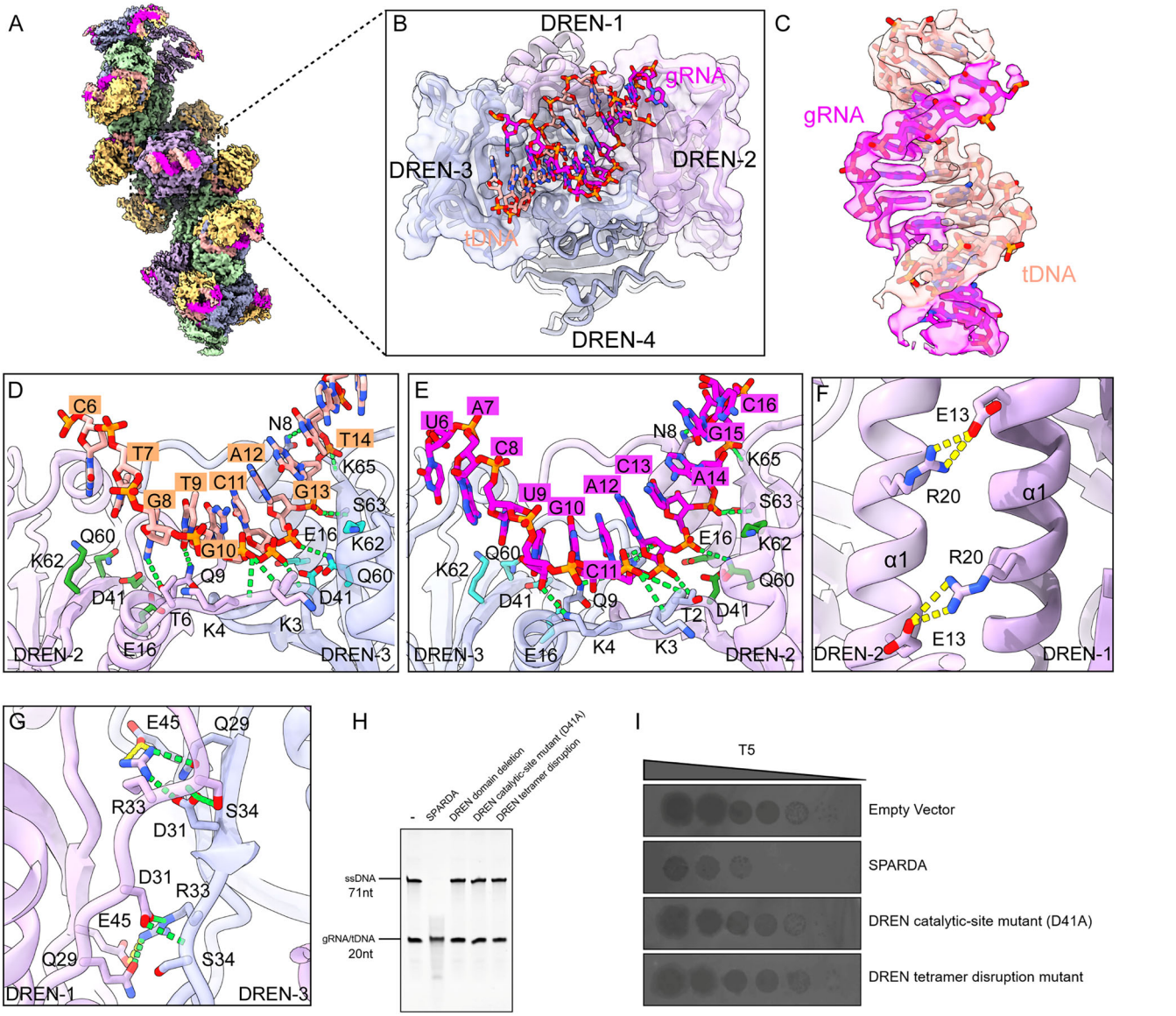

Fig. 4 | The mechanism of SPARDA activation. (**A**) Density of gRNA–tDNA SPARDA. **B** Enlarged view of the cryo-EM density of the nucleic acids within the DREN domain. **C** Density of the gRNA–tDNA duplex. **D**, **E** Interaction details between the DREN and substrate. Hydrogen bonds are indicated by green dashed lines. The catalytic site of DREN-2 is coloured green, and the catalytic site of DREN-3 is coloured cyan. **F** Tetramerization of DREN mediated by the α1-helix of DREN. (**G**) The tetramerization of the DREN mediated by the β1β2–β1β2 interfaces within DREN. Hydrogen bonds and salt bridges are indicated by green and orange dashed lines, respectively. **H** Collateral activity of *Nba*SPARDA and the mutants with ssDNA. The gel image is representative of three independent experiments with similar results. **I** Plaque assay with 10-fold serial dilutions using T5 to infect *E. coli* expressing the wild-type SPARDA and mutants on the catalytic sites and the residues responsible for tetramerization of DREN.

exposed to the other side of DREN (Fig. 4B). Additionally, two regions of extra density are observed in the DREN domain, which can be assigned as the gRNA–tDNA duplex (Fig. 4C). The RNA–DNA duplex is stabilized by interactions between phosphate groups and residues within the activated DREN domain (Fig. 4D, E). Specifically, the binding of tDNA and gRNA to the DREN2 and DREN3 domains exhibits a mirror-image relationship. This structural arrangement allows tDNA to enter the catalytic amino acid pocket of DREN3, which is composed of residues E16, D41, Q60, and K62, while the gRNA simultaneously occupies the corresponding catalytic pocket in DREN2 (Fig. 4D, E). This configuration highlights the structural consistency underlying the recognition and cleavage of a broad spectrum of nucleic acid substrates.

To elucidate the molecular basis of DREN tetramer assembly, we characterized the intermolecular interactions among DREN protomers. DREN-1, DREN-2 and DREN-3 are utilized to analyse their interactions. Structural analysis revealed that these two regions predominantly contributed to their interactions. Specifically, the adjacent DREN protomers engage through their α1 helices, bringing residues E13 and R20 into proximity. Reciprocal hydrogen bonds form between E13 of one protomer and R20 of its neighbour, and vice versa, thereby stabilizing helix–helix packing (Fig. 4F). Moreover, the β-sheet core of DREN-1 is oriented towards the β-sheet of DREN-3, forming interfacial interactions mediated by the residues in the β1–β2 strands of DREN-2. At the β1–β2 interface, residues located on β1 and β2 and the loop connecting them to the DREN molecule form a hydrogen bond network with the same regions in the other DREN. Specifically, D31 on β1 and E45 on β2 of DREN2 form hydrogen bonds with R33 on the β1–β2 loop and Y88 on α2 of DREN3, respectively. Additionally, R33 on the β1–β2 loop of DREN2 forms hydrogen bonds with D31 and E45 on β2 of

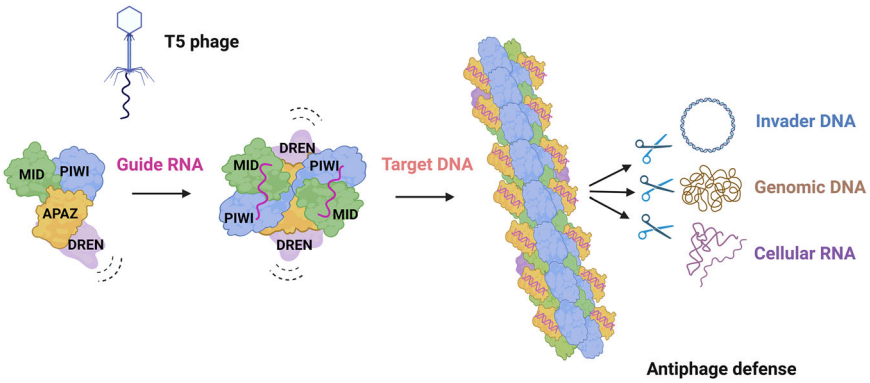

Fig. 5 | Proposed model for the SPARDA system. Proposed model describing the filament induced by the binding of tDNA. The SPARDA heterodimer can recognize gRNA, which becomes a dimer, and the sequential recognition of tDNA can stimulate the filamentation of SPARDA, thereby activating nuclease activity by means of the tetramerization of the DREN domain, thus conferring resistance against T5 phage infection. Created in BioRender. Wanyue, Z. (2025) https:// BioRender.com/szi9dc7.

DREN3 (Fig. 4G). Structural homology analysis using Dali revealed that the endonuclease I-Ssp6803I is most similar to DREN. Notably, I-Ssp6803I also adopts a D2-symmetric tetrameric arrangement to cleave double-stranded DNA (dsDNA)[27] (Supplementary Fig. 9B).

In the apo SPARDA, as predicted by AlphaFold3, the N-terminal DREN was located outside the gRNA–tDNA binding channel. Similarly, in the gRNA–bound SPARDA complex, although the DREN domains themselves were unresolved in the structure, the orientations of their linkers suggested that the two DREN domains were spatially separated (Fig. 1C). In the activated SPARDA–gRNA–tDNA filament, the four DREN molecules exhibit nearly identical conformations to each other, but they are stabilized and further oligomerized within the SPARDA filament induced by tDNA recognition. Deletion of the DREN domain did not alter the filament formation induced by tDNA recognition and the gRNA according to the SEC elution file and the corresponding appearance on the micrographs (Supplementary Fig. 10). Based on these observations, we proposed that SPARDA filament-driven tetramerization of DREN is critical for its nuclease activity. We subsequently performed structure-guided mutagenesis of these interacting residues involved in DREN oligomerization. The results revealed that single-point mutations had a negligible impact, however, group alanine substitution on the resides involved in tetramerization (E13A/N17A/R20A/R33A/Q29A/E45A) significantly abolished both the nuclease activity against the substrate according to the in vitro nuclease assays and its capacity to defend against bacteriophages (Fig. 4H, I, Supplementary Fig. 11). Taken together, these findings demonstrate that the unique filament architecture of SPARDA drives DREN oligomerization, which is indispensable for substrate recognition and catalytic function (Fig. 5).

Discussion

Recent studies have demonstrated that pAgo family proteins, particularly short pAgos, play an essential role in combating phage infections[11,13,23]. A featured characteristic of the pAgo systems is that the effector domains are fused to the APAZ domain via a long linker encoded by the pAgo-associated partner, whose enzymatic activities are obtained upon the recognition of guide and target nucleic acids. SPARTA, SPARSA and SPARDA belong to different phylogenetic clades. Both SPARTA and SPARSA utilize NADase-containing effectors that hydrolyse NAD^+ upon RNA-guided recognition of target DNA, thereby leading to cell death to provide resistance against phage infections. Subsequent structural studies revealed that inactive SPARTA[17] and SPARSA[19] adopt a monomer in solution in the absence of target nucleic acids. The activation of their NADase activity depends on the tetramerization of the TIR domain in SPARTA and the Sir2 domain in SPARSA, which is induced by target ssDNA binding. In SPARTA and SPARSA, the active tetrameric architecture is formed by interfaces involving the pAgo subunit and the enzymatic domains located outside of the nucleic acid-binding channel. In SPARDA, the activation of the nuclease of DREN relies on its assembly into filaments upon the recognition of the guide RNA and target DNA. The tetramerization-dependent activation of DREN is similar to those of SPARTA and SPARSA, in which the Sir2 and TIR domains assemble into a tetramer upon nucleic acid binding. Dali search server reveals that the structure of the DREN domain within SPARDA is similar to type II restriction endonuclease. Most of these restriction enzymes function as homodimers possessing two catalytic sites, a structural feature that appears to facilitate the binding and efficient cleavage of palindromic substrate sites. In addition, tetrameric assemblies are also common among type II restriction endonucleases, such as NgoMIV and SfiI. Structurally, these tetramers typically form through the head-to-head stacking of two dimers. In this manner, the two DNA-bound dimers in the restriction endonuclease place the PD-(D/E)-XK domains, their DNA-binding surfaces and the active sites close together in the individual protein. In contrast, the tetrameric I-SspI is able to accumulate a single long substrate and allows the catalytic PD-(D/E)-XK to far apart, thereby cleaving a long target site. The tetramer assembly of the SPARDA DREN domain induced by ssDNA recognition can accumulate the substrate, thereby avoiding the undesired activation under physiological conditions. AlphaFold-predicted structures indicated that the DREN domain resides outside the nucleic acid-binding cleft[24]. The authors speculated that conformational rearrangements might occur in this region upon nucleic acid recognition to activate its nuclease function[24]. Here, using cryo-EM, we reveal a novel mechanism by which tDNA binding triggers the filamentation of SPARDA, a phenomenon that has not been reported in other pAgos. Critically, filament formation is essential for SPARDA's nuclease activity. Within this supramolecular structure, the DREN domain undergoes tetramerization, thereby creating a catalytic pocket capable of substrate binding and hydrolysing nucleic acids. In particular, in our study, the annealing of gRNA and tDNA generated an RNA–DNA heteroduplex, which was captured by the DREN tetramer within the SPARDA filament. This provides an explanation for the nuclease activity of SPARDA towards the RNA–DNA duplex[24].

Intriguingly, recent studies have revealed that filament assembly is dependent on the activation of antiphage effectors and is a widely used strategy in multiple antiphage defence systems[28–32]. In Thoeris, the binding of 1″-3′ glycocyclic ADP ribose (gcADPR) to the SLOG domain of ThsA induced the filamentation of ThsA tetramers, which stabilized the active conformation of its Sir2 domain and prevented

steric hindrance between the catalytic pocket and the substrate[28]. In the most widespread type of CBASS, the inactive dimeric phospholipase effector CapE was activated and formed a higher-order filament upon the cyclic dinucleotides. In the activated CapE filament, the α7 helix transforms into a flexible loop to open the entrance of the substrate to the catalytic site[32]. In the type II-C CBASS antiviral system[33], the signalling cGAMP binds at the STING interface, driving filament formation due to the stacking of dimeric STING units[34]. Consequently, tetramerization of the adjacent TIR domain in the TIR–STING filament generates an NAD^+-binding catalytic pocket[33,34]. Additionally, in Type III CRISPR systems, Cat1 features an N-terminal TIR domain and a C-terminal CARF domain. Binding of the signalling molecule cA4 to CARF domains induces cooperative dimer stacking, ultimately driving helical filament assembly[35]. Filament formation repositions TIR domains into spatial proximity, resulting in the construction of a catalytic pocket that is competent for NAD^+ hydrolysis[35].

During the manuscript preparation, similar research on the activation mechanism of *Nba*SPARDA was published[36]. In their study, most of the results, including the filament assembly of SPARDA induced by tDNA binding and the collateral nuclease activity dependent on the tetramerization of DREN induced by the filament of SPARDA, were consistent with our study[36]. However, the substrate bound to the DREN domain was ssDNA instead of the gRNA–tDNA heteroduplex in our study. Like *Nba*SPARDA, the activation of *Xau*SPARDA from *Xanthobacter autotrophicus* strain Py2 is also dependent on filament assembly upon the binding of tDNA[37]. In addition, a preprint study on anther clades on short pAgos–SPARHA (short prokaryotic Argonautes, HNH-associated) also revealed that filament formation was caused by tDNA binding[38]. Collectively, these findings establish that tDNA binding triggers helical filament assembly in SPARDA, which represents a novel paradigm within the filament-mediated antiphage defence framework.

Methods

Plasmid construction

The *Nba*Ago gene (GenBank accession: WP_022673743.1) and the DREN-APAZ gene (WP_033317603.1) from the NCBI database were synthesized by Sangon Biotech (Shanghai, China). For expression of the *Nba*Ago/DREN-APAZ complex in *E. coli*, His-tagged *Nba*Ago and S-tagged DREN-APAZ were cloned into the first and second multiple cloning sites of pETDuet-1, respectively. Site-directed mutagenesis to generate mutant complexes was performed on the *Nba*Ago/DREN-APAZ protein-expression plasmid using whole-plasmid PCR amplification. The nucleic acid sequences used in this study are listed in Supplementary Data 1.

Protein expression and purification

The corresponding recombinant plasmids were transformed into *E. coli* BL21(DE3) cells. The transformants were inoculated in LB medium supplemented with 100 μM Amp and grown for approximately 6 h at 37 °C. When the OD_{600} reached 0.6–0.8, the cultures were induced with 0.4 mM IPTG and shifted to 16 °C for 16-18 h. The cells were collected by centrifugation and resuspended in buffer containing 20 mM Tris-HCl, pH 8.0, and 500 mM NaCl. After lysis by sonication on ice, the lysate was centrifuged at 17,000 × *g* for 30 min at 4 °C. The supernatant was then loaded onto a Ni^{2+}-NTA column (Qiagen) pre-equilibrated with lysis buffer. The column was washed with 10 column volumes (CV) of equilibration buffer to remove unbound proteins. This was followed by a wash with 10 CV of equilibration buffer supplemented with 20 mM imidazole to remove weakly bound contaminants. Finally, the His-tagged protein complex was eluted with equilibration buffer supplemented with 300 mM imidazole. The eluate was then diluted fivefold with a buffer containing 20 mM Tris-HCl (pH 8.0) and 5 % glycerol. The supernatant was loaded onto a 5 ml heparin-Sepharose column (Cytiva) pre-equilibrated with buffer containing 20 mM Tris-HCl (pH 8.0), 150 mM NaCl, and 2 mM DTT. The column was washed with the same buffer, and the protein complex was eluted using a linear NaCl gradient (from 150 mM to 1 M) in the identical buffer. Subsequently, the eluted protein was concentrated to 0.5 ml using a 30K-cutoff concentrator (Millipore), which was purified with a Superdex 200 increase column (Cytiva) equilibrated with buffer containing 20 mM Tris-HCl (pH 8.0), 150 mM NaCl and 2 mM DTT. The major chromatographic peak was fractionated in 0.5 ml aliquots, pooled, and concentrated for storage at −20 °C. Mutant complexes were purified following the same procedure as described above.

In vitro assembly of the SPARDA-gRNA-tDNA complex

To assemble SPARDA-gRNA complex, the purified SPARDA complex was incubated with guide RNA and target DNA at a molar ratio of 1:2:2. The mixture was then incubated at 4 °C for 30 min and loaded onto a Superdex 200 increase column (Cytiva). Fractions containing the SPARDA-gRNA-tDNA complex were pooled, flash frozen in liquid nitrogen, and stored at −80 °C.

Analytical ultracentrifugation (AUC)

Sedimentation velocity experiments were performed using an Optima analytical ultracentrifuge (Beckman Coulter, Inc, Brea, CA, USA) equipped with an absorbance optical system set to 280 nm. Samples were loaded into double-sector centerpieces and analyzed in an An-60 Ti rotor at 45,000 × g and 10 °C. All measurements were conducted in a buffer containing 20 mM Tris-HCl (pH 8.0) and 150 mM NaCl. The following complexes were characterized: (i) SPARDA complex, (ii)the gRNA-bound SPARDA complex, and (iii) the gRNA-tDNA SPARDA complex. Data were acquired at 280 nm with a radial spacing of 0.003 cm. Sedimentation coefficient distributions [c(s)] were determined using SEDFIT software (version 16.1c) with default parameters.

Cryo-EM sample preparation and data collection

For the SPARDA-gRNA complex dataset, aliquots (3 μL) of a 1.8 mg/mL mixture were loaded onto glow-discharged (80 s at 20 mA) holey carbon Quantifoil grids (AU 2/1, 300 mesh, Quantifoil Micro Tools) using a Vitrobot Mark IV (Thermo Fisher Scientific) at 100% humidity and 4 °C. For the SPARDA-gRNA-tDNA complex dataset, the sample was prepared and vitrified under identical conditions. All data were acquired using the EPU software on Titan Krios G4 transmission electron microscopy (Thermo Fisher Scientific) operated at 300 kV. Images were recorded using a Gatan K3 detector in a 48-frame movie mode at a nominal 130,000× magnification with a pixel size of 0.325 Å, and the total electron dose was set to 48 $e^-·Å^{-2}$, with an exposure time of 1.35 s.

Image processing and 3D reconstruction

Drift and beam-induced motion correction were performed with MotionCor2[39] to produce a micrograph from each movie. Contrast transfer function (CTF) fitting and phase-shift estimation were conducted with Gctf[40]. Micrographs with astigmatism, obvious drift, or contamination were discarded before reconstruction. The following reconstruction procedures were performed using Cryosparc V3[41]. In brief, particles were automatically picked using the "Blob picker" or "Filament Tracer". Several rounds of reference-free 2D classifications were performed and the selected "good" particles were then subjected to ab initio reconstruction, heterogeneous refinement, and final non-uniform refinement. Localized refinement focusing of the local areas, were also performed if necessary. The resolutions of all density maps were determined by the gold-standard Fourier shell correlation curve, with a cutoff of 0.1434[42]. Local resolutions of maps were estimated with ResMap[43].

Atomic model building, refinement, and 3D visualization

The initial models of the *Nba*SPARDA complex were acquired from Alphafold3[44]. We initially fitted the models into the corresponding final cryo-EM maps using Chimera[45], and further corrected and adjusted them manually by real-space refinement in Coot[46]. The resulting models were then refined with phenix.real_space_refine in PHENIX[47]. These operations were executed iteratively until the problematic regions, Ramachandran outliers, and poor rotamers were either eliminated or moved to favoured regions. The final atomic models were validated with Molprobity[48]. All structural figures were generated with ChimeraX[45].

Phage Efficiency of Plating (EOP) Assay

The efficiency of plating (EOP) assay was performed using *E. coli* BL21(DE3) cells harbouring the pET-Duet-1 vector expressing wild-type or mutant SPARDA. For the spot assay, overnight cultures of the expression strain were diluted 1:100 in MMB medium (LB supplemented with 0.1 mM $MnCl_2$, 5 mM $MgCl_2$, 5 mM $CaCl_2$) containing 0.5% agar and grown at 37°C with shaking until OD_{600} reached 0.3. Protein expression was induced with 0.3 mM IPTG, and incubation continued until OD_{600} reached 0.6. Then, 500 µl of induced culture was mixed with 20 mL of molten MMB medium containing 0.2 mM IPTG and 100 µg/mL ampicillin to form bacterial lawns. Serially diluted phage T5 lysates (10-fold gradients) in MMB medium were spotted (4 µl per droplet) onto the lawns. Plates were incubated at room temperature for 24 hours before plaque counting and analysis.

Cleavage assays

Cleavage assays were performed to determine the activity of the SPARDA complex toward ssDNA, dsDNA and RNA substrates under various reaction conditions. Typically, 500 nM SPARDA complex was preincubated with 200 nM guide RNA for 15 min at 37 °C in a buffer containing 20 mM Tris-HCl (pH 8.0), 0.1 mg/ml BSA, 2 mM DTT and 10 mM Mg^{2+}. Subsequently, 200 nM target DNA was added to the reaction mixture, followed by an additional 15 minute incubation. Substrate oligonucleotides (ssDNA, dsDNA and RNA) were then added to a final concentration of 100 nM. The reactions were incubated for 30 min, and then an equal volume of loading buffer containing 8 M urea, 20 mM EDTA and 2× TBE prepared from a commercial 10× TBE stock (Invitrogen). Reaction products were separated by 20% denaturing polyacrylamide gel (containing 8 M urea) and visualized by staining with SYBR Gold and scanning using an Amersham Typhoon imager (Cytiva).

Bimolecular fluorescence complementation assays

The superfolder green fluorescent protein (sfGFP) reporter was split into two distinct fragments: the large β1–β10 barrel (residues 1-214) and the small β11 strand (residues 215-239). The sfGFP β1–β10 fragment was fused to the DREN. Subsequently, an expression cassette encoding the sfGFP β1–β10-DREN-APAZ, and pAgo was cloned into the multiple cloning site of the pRSF-Duet-1 vector. Similarly, the sfGFP β11 fragment was fused to DREN, and the corresponding sfGFP β11-DREN-APAZ-pAgo cassette was assembled into the pET-Duet-1 vector. These two recombinant plasmids were then co-transformed with a third plasmid, pCDFDuet-1, into *E. coli* BL21(DE3) competent cells. Positive transformants were selected on LB agar plates containing ampicillin, kanamycin, and spectinomycin. A single colony was inoculated into LB liquid medium supplemented with the same antibiotics and grown at 37°C with shaking until the OD_{600} reached ~0.6. Protein expression was induced by adding 0.3 mM IPTG, followed by incubation at 16°C for 16 h. Finally, cells were then harvested and resuspended in PBS buffer, and subjected to imaging using a Leica STELLARIS confocal microscope.

Reporting summary

Further information on research design is available in the Nature Portfolio Reporting Summary linked to this article.

Data availability

The cryo-EM map of SPARDA has been deposited in the Electron Microscope Data Band (EMDB) with the accession code EMD-65405 [https://www.ebi.ac.uk/pdbe/entry/emdb/ EMD-65405] and EMD-65406 [https://www.ebi.ac.uk/pdbe/entry/emdb/ EMD-65406]. The atomic coordinates and structure factors of SPARDA have been deposited in the PDB (Protein Data Bank) under the accession codes 9VX1 and 9VX6. Source data are provided with this paper.

References

1. Elbashir, S. M., Lendeckel, W. & Tuschl, T. RNA interference is mediated by 21- and 22-nucleotide RNAs. *Genes Dev.* **15**, 188–200 (2001).
2. Iwakawa, H. O. & Tomari, Y. Life of RISC: Formation, action, and degradation of RNA-induced silencing complex. *Mol. Cell* **82**, 30–43 (2022).
3. Song, J. J., Smith, S. K., Hannon, G. J. & Joshua-Tor, L. Crystal structure of Argonaute and its implications for RISC slicer activity. *Science* **305**, 1434–1437 (2004).
4. Frank, F., Sonenberg, N. & Nagar, B. Structural basis for 5′-nucleotide base-specific recognition of guide RNA by human AGO2. *Nature* **465**, 818–822 (2010).
5. Wang, C., Shen, Z., Yang, X. Y. & Fu, T. M. Structures and functions of short argonautes. *RNA Biol.* **21**, 1–7 (2024).
6. Wang, Y. et al. Structure of an argonaute silencing complex with a seed-containing guide DNA and target RNA duplex. *Nature* **456**, 921–926 (2008).
7. Swarts, D. C. et al. The evolutionary journey of Argonaute proteins. *Nat. Struct. Mol. Biol.* **21**, 743–753 (2014).
8. Lisitskaya, L., Aravin, A. A. & Kulbachinskiy, A. DNA interference and beyond: structure and functions of prokaryotic Argonaute proteins. *Nat. Commun.* **9**, 5165 (2018).
9. Chen, Y., Zeng, Z., She, Q. & Han, W. The abortive infection functions of CRISPR-Cas and Argonaute. *Trends Microbiol.* **31**, 405–418 (2023).
10. Ryazansky, S., Kulbachinskiy, A. & Aravin, A. A. The Expanded Universe of Prokaryotic Argonaute Proteins. *mBio* **9**, https://doi.org/10.1128/mBio.01935-18 (2018).
11. Koopal, B. et al. Short prokaryotic Argonaute systems trigger cell death upon detection of invading DNA. *Cell* **185**, 1471–1486 e1419 (2022).
12. Zhang, H. et al. Structural insights into activation mechanisms on NADase of the bacterial DSR2 anti-phage defense system. *Sci. Adv.* **10**, eadn5691 (2024).
13. Zaremba, M. et al. Short prokaryotic Argonautes provide defence against incoming mobile genetic elements through NAD(+) depletion. *Nat. Microbiol.* **7**, 1857–1869 (2022).
14. Shen, Z. et al. Oligomerization-mediated activation of a short prokaryotic Argonaute. *Nature* **621**, 154–161 (2023).
15. Ni, D., Lu, X., Stahlberg, H. & Ekundayo, B. Activation mechanism of a short argonaute-TIR prokaryotic immune system. *Sci. Adv.* **9**, eadh9002 (2023).
16. Guo, L. et al. Auto-inhibition and activation of a short Argonaute-associated TIR-APAZ defense system. *Nat Chem Biol*, https://doi.org/10.1038/s41589-023-01478-0 (2023).
17. Zhang, J. T., Wei, X. Y., Cui, N., Tian, R. & Jia, N. Target ssDNA activates the NADase activity of prokaryotic SPARTA immune system. *Nat. Chem. Biol.* **20**, 503–511 (2024).
18. Gao, X. et al. Nucleic-acid-triggered NADase activation of a short prokaryotic Argonaute. *Nature* **625**, 822–831 (2024).

19. Zhen, X. et al. Structural basis of antiphage immunity generated by a prokaryotic Argonaute-associated SPARSA system. *Nat. Commun.* **15**, 450 (2024).
20. Cui, N. et al. Tetramerization-dependent activation of the Sir2-associated short prokaryotic Argonaute immune system. *Nat. Commun.* **15**, 8610 (2024).
21. Sun, D. et al. Nucleic acid-induced NADase activation of a short Sir2-associated prokaryotic Argonaute system. *Cell Rep.* **43**, 114391 (2024).
22. Wang, X. et al. Structural insights into mechanisms of Argonaute protein-associated NADase activation in bacterial immunity. *Cell Res.* **33**, 699–711 (2023).
23. Zeng, Z. et al. A short prokaryotic Argonaute activates membrane effector to confer antiviral defense. *Cell Host Microbe* **30**, 930–943 e936 (2022).
24. Prostova, M. et al. DNA-targeting short Argonautes complex with effector proteins for collateral nuclease activity and bacterial population immunity. *Nat. Microbiol.* **9**, 1368–1381 (2024).
25. Lu, X., Xiao, J., Wang, L., Zhu, B. & Huang, F. The nuclease-associated short prokaryotic Argonaute system nonspecifically degrades DNA upon activation by target recognition. *Nucleic Acids Res.* **52**, 844–855 (2024).
26. Guo, L. et al. Auto-inhibition and activation of a short Argonaute-associated TIR-APAZ defense system. *Nat. Chem. Biol.* **20**, 512–520 (2024).
27. Zhao, L., Bonocora, R. P., Shub, D. A. & Stoddard, B. L. The restriction fold turns to the dark side: a bacterial homing endonuclease with a PD-(D/E)-XK motif. *EMBO J.* **26**, 2432–2442 (2007).
28. Tamulaitiene, G. et al. Activation of Thoeris antiviral system via SIR2 effector filament assembly. *Nature* **627**, 431–436 (2024).
29. Wang, Y., Tian, Y., Yang, X., Yu, F. & Zheng, J. Filamentation activates bacterial Avs5 antiviral protein. *Nat. Commun.* **16**, 2408 (2025).
30. Smalakyte, D., Ruksenaite, A., Sasnauskas, G., Tamulaitiene, G. & Tamulaitis, G. Filament formation activates protease and ring nuclease activities of CRISPR Lon-SAVED. *Mol. Cell* **84**, 4239–4255 e4238 (2024).
31. Wang, Y. et al. DNA methylation activates retron Ec86 filaments for antiphage defense. *Cell Rep.* **43**, 114857 (2024).
32. Wang, J. et al. Cyclic-dinucleotide-induced filamentous assembly of phospholipases governs broad CBASS immunity. *Cell*, https://doi.org/10.1016/j.cell.2025.04.022 (2025).
33. Morehouse, B. R. et al. Cryo-EM structure of an active bacterial TIR-STING filament complex. *Nature* **608**, 803–807 (2022).
34. Hogrel, G. et al. Cyclic nucleotide-induced helical structure activates a TIR immune effector. *Nature* **608**, 808–812 (2022).
35. Baca, C. F., Majumder, P., Hickling, J. H., Patel, D. J. & Marraffini, L. A. Cat1 forms filament networks to degrade NAD(+) during the type III CRISPR-Cas antiviral response. *Science*, eadv9045, https://doi.org/10.1126/science.adv9045 (2025).
36. Wang, F., Xu, H., Zhang, C., Xue, J. & Li, Z. Target DNA-induced filament formation and nuclease activation of SPARDA complex. *Cell Res.*, https://doi.org/10.1038/s41422-025-01100-z (2025).
37. Jurgelaitis, E. et al. Activation of the SPARDA defense system by filament assembly using a beta-relay signaling mechanism widespread in prokaryotic Argonautes. *Cell Res.* **35**, 1056–1078 (2025).
38. Kanevskaya, A. et al. Argonaute-HNH filaments triggered by invader DNA confer bacterial immunity. *Nat. Commun.* https://doi.org/10.1038/s41467-025-66189-7 (2025).
39. Zheng, S. Q. et al. MotionCor2: anisotropic correction of beam-induced motion for improved cryo-electron microscopy. *Nat. Methods* **14**, 331–332 (2017).
40. Zhang, K. Gctf: Real-time CTF determination and correction. *J. Struct. Biol.* **193**, 1–12 (2016).
41. Punjani, A., Rubinstein, J. L., Fleet, D. J. & Brubaker, M. A. cryoSPARC: algorithms for rapid unsupervised cryo-EM structure determination. *Nat. Methods* **14**, 290–296 (2017).
42. Scheres, S. H. & Chen, S. Prevention of overfitting in cryo-EM structure determination. *Nat. Methods* **9**, 853–854 (2012).
43. Kucukelbir, A., Sigworth, F. J. & Tagare, H. D. Quantifying the local resolution of cryo-EM density maps. *Nat. Methods* **11**, 63–65 (2014).
44. Abramson, J. et al. Accurate structure prediction of biomolecular interactions with AlphaFold 3. *Nature* **630**, 493–500 (2024).
45. Meng, E. C. et al. UCSF ChimeraX: Tools for structure building and analysis. *Protein Sci.* **32**, e4792 (2023).
46. Emsley, P. & Cowtan, K. Coot: model-building tools for molecular graphics. *Acta Crystallogr. D. Biol. Crystallogr.* **60**, 2126–2132 (2004).
47. Adams, P. D. et al. PHENIX: a comprehensive Python-based system for macromolecular structure solution. *Acta Crystallogr. D. Biol. Crystallogr.* **66**, 213–221 (2010).
48. Chen, V. B. et al. MolProbity: all-atom structure validation for macromolecular crystallography. *Acta Crystallogr. D. Biol. Crystallogr.* **66**, 12–21 (2010).

Acknowledgements

This work was supported by the National Nature Science Foundation of China grants (82225028, U25A20131, 92581119, 32170045, 82172287, 82341085, and 32570035), the Nature Science Foundation of Fujian Province (2023J06026 and 2023J0123), Prevention and Control of Emerging and Major Infectious Diseases-National Science and Technology Major Project (2025ZD01903600) and the High-level personnel introduction grant of Fujian Normal University (Z0210509). We thank the staff at the Cryo-EM Facilities of Xiamen University for the data collection.

Author contributions

X.Z., Q.Z., and S.O. conceived the project and designed the experiments. W.Z. and S.X. prepared the samples, and W.Z. performed most of the biochemical experiments. Y.J., Y.L. and X.W. collected the cryo-EM data. X.W., Y.L. analyzed and calculated the EM map and built and regained the atomic model. N. X., and S. L. discussed and analyzed the results. X.Z. wrote the manuscript with support from all the authors.

Competing interests

The authors declare no competing interests.

Additional information

Supplementary information The online version contains supplementary material available at https://doi.org/10.1038/s41467-025-68195-1.

Correspondence and requests for materials should be addressed to Shaowei Li, Xurong Wang, Qingbing Zheng or Songying Ouyang.

Peer review information *Nature Communications* thanks Babatunde Ekundayo and the other anonymous reviewer(s) for their contribution to the peer review of this work. A peer review file is available.